Geophysical Research Letters

RESEARCH LETTER
10.1029/2022GL098582

Topographic Control on Ground Motions and Landslides From the 2015 Gorkha Earthquake

Audrey M. Dunham[1], Eric Kiser[1], Jeffrey S. Kargel[2], Umesh K. Haritashya[3], C. Scott Watson[4], Dan H. Shugar[5], Amanda Hughes[1], and Peter G. DeCelles[1]

[1]Department of Geoscience, University of Arizona, Tucson, AZ, USA, [2]Planetary Science Institute, Tucson, AZ, USA, [3]Department of Geology and Environmental Geosciences, University of Dayton, Dayton, OH, USA, [4]COMET, School of Earth and Environment, University of Leeds, Leeds, UK, [5]Water, Sediment, Hazards, and Earth-surface Dynamics (waterSHED) Lab, Department of Geoscience, University of Calgary, Calgary, AB, Canada

Abstract Landslides triggered by earthquake shaking pose a significant hazard in active mountain regions. Steep topography promotes gravitational instabilities and can amplify the seismic wavefield; however, the relationship between topographic amplification and landsliding is poorly understood. Here, we use numerical methods to investigate the link between low-frequency ground shaking, topographic amplification, and the landslide distribution from the 2015 Gorkha, Nepal earthquake. Results show that the largest landslides initiated where the highest topographic amplification, highest elevations, and steepest slopes converged, typically in glacially-sculpted terrain, with additional controls of rock strength and absolute ground motions. Additionally, the initiation of the largest and most fatal landslide was likely influenced by amplification throughout the rupture due the orientation of the ridge with respect to the propagating wavefield. These results indicate that topographic amplification is one of the key factors for understanding where large and potentially devastating landslides are likely to occur during future major earthquakes.

Plain Language Summary Coseismic landslides, or landslides that happen because of earthquake shaking, can cause more damage and devastation to communities than the earthquake shaking itself. One potential cause of coseismic landslide initiation is increased seismic amplitudes at the tops of ridges due to constructive interference of seismic waves within a ridge, a phenomenon known as topographic amplification. The shaking from the 2015 Gorkha earthquake in Nepal caused 25,000 coseismic landslides. In this study, we model the ground shaking caused by the earthquake to isolate how topography affects the amplitudes of seismic waves and whether this contributed to landsliding. We find that topographic amplification plays an important role in initiating the largest landslides and that continual amplification of one ridge throughout the earthquake influenced the initiation of the largest and most fatal landslide. Modeling topographic amplification from future earthquakes could improve our estimates of where the largest and most devastating landslides are likely to occur.

Key Points:

- Initiation of the largest coseismic landslides corresponds to high topographic amplification, steep slopes, and high elevations
- The initiation of the Langtang Valley landslide was likely influenced by multiple episodes of amplification throughout the rupture
- Characterizing topographic amplification can provide insight into where large landslides are likely to occur during future earthquakes

Supporting Information:

Supporting Information may be found in the online version of this article.

Correspondence to:

A. M. Dunham,
amd95@email.arizona.edu

Citation:

Dunham, A. M., Kiser, E., Kargel, J. S., Haritashya, U. K., Watson, C. S., Shugar, D. H., et al. (2022). Topographic control on ground motions and landslides from the 2015 Gorkha earthquake. *Geophysical Research Letters*, *49*, e2022GL098582. https://doi.org/10.1029/2022GL098582

Received 7 MAR 2022
Accepted 5 MAY 2022

Author Contributions:

Conceptualization: Eric Kiser, Jeffrey S. Kargel, Umesh K. Haritashya
Formal analysis: Audrey M. Dunham, C. Scott Watson
Funding acquisition: Eric Kiser, Jeffrey S. Kargel, Umesh K. Haritashya
Investigation: Peter G. DeCelles
Methodology: Audrey M. Dunham, Eric Kiser
Resources: Amanda Hughes
Software: Amanda Hughes
Supervision: Eric Kiser
Validation: Audrey M. Dunham
Visualization: Audrey M. Dunham
Writing – original draft: Audrey M. Dunham
Writing – review & editing: Eric Kiser, Jeffrey S. Kargel, Umesh K. Haritashya, C. Scott Watson, Dan H. Shugar, Amanda Hughes, Peter G. DeCelles

1. Introduction

Landslides caused by seismic shaking are a major secondary hazard of large earthquakes (Keefer, 2002; Petley, 2012). In general, topography plays an important role in triggering coseismic landslides by setting the first-order susceptibility of the slope to failure and amplifying/de-amplifying the seismic wavefield produced by local earthquakes. Ridges, in particular, tend to focus seismic energy through the interactions of scattered waves, a phenomenon known as topographic amplification (Asimaki & Mohammadi, 2018; Hartzell et al., 2017; Lee et al., 2009; Maufroy et al., 2015). Previous studies have investigated the distribution of earthquake-induced landslides, either coseismic or post-seismic landslides, with respect to ridge tops with various lithologies and rock strengths (Rault et al., 2019), as well as general relationships between the shapes of ridges and seismic amplification (Rault et al., 2020). However, the lack of dense instrumentation in regions of rugged topography, such as the Himalaya, has hindered progress in understanding the relationships between the characteristics of coseismic landslides and the seismic wavefields from the large earthquakes that promoted these landslides.

The 25 April 2015 M_w 7.8 Gorkha, Nepal earthquake occurred ~80 km NW of Kathmandu and ruptured primarily along a gently dipping detachment portion of the Main Himalaya Thrust (MHT) (Figures 1a and 1c) (Hubbard et al., 2016). Source imaging and slip modeling of this event show a unilateral rupture propagating ~150 km to the E/SE of the mainshock epicenter within the lower locked portion of the MHT, with highest slip occurring in the center of the rupture just north of Nepal's capital, Kathmandu (Avouac et al., 2015; Fan & Shearer, 2015; Wei

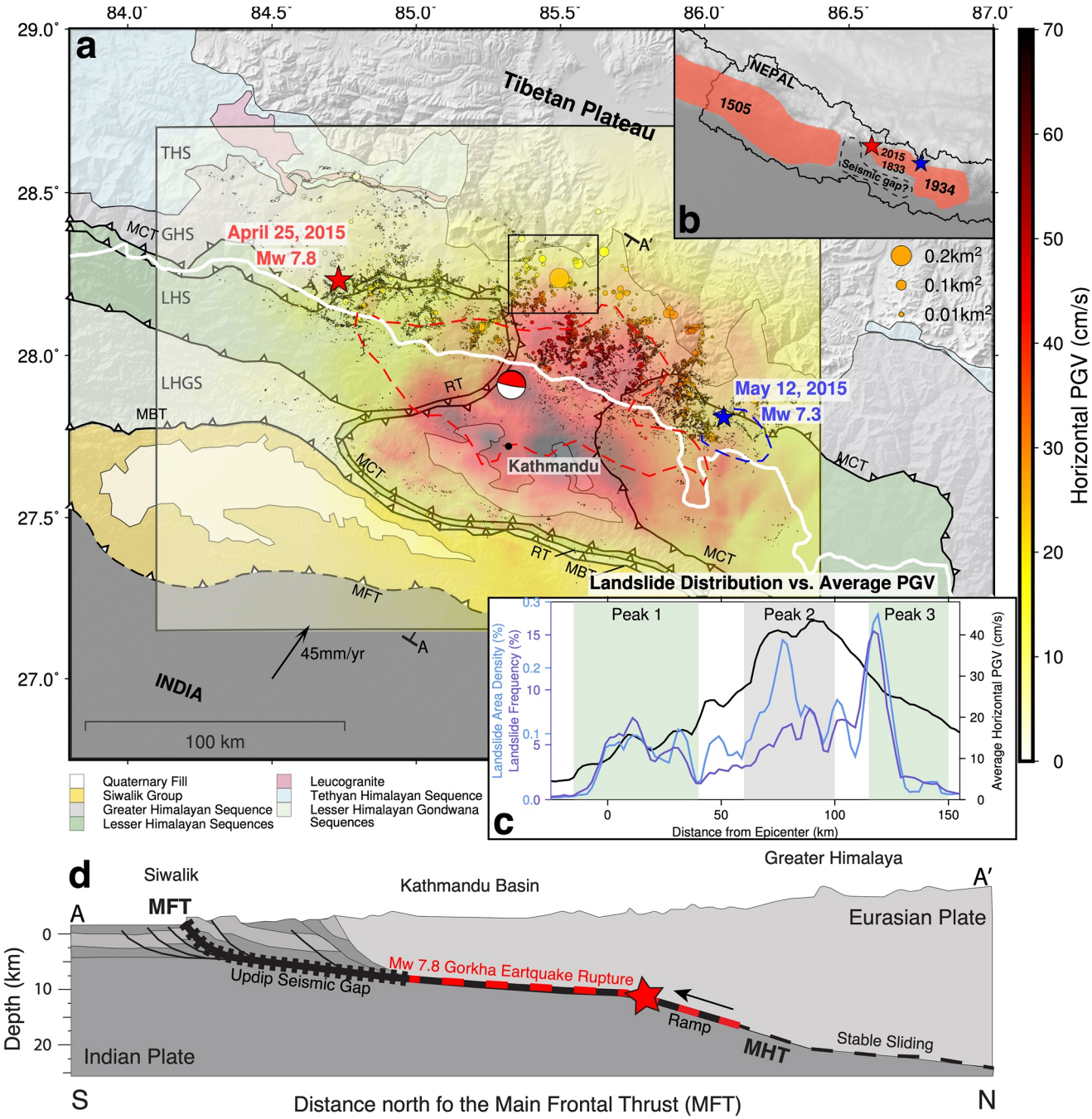

Figure 1.

et al., 2018) (slip model in Figure S1 in Supporting Information S1). The most comprehensive landslide catalog from this event (Roback et al., 2018), used in this study, includes ~25,000 landslides characterized by source location, size, and extent of landslide runout. Strong ground motion data are not available in the regions of high density landsliding from this event, making it impossible to directly relate ground shaking and landslide distribution. In lieu of this direct comparison, we use the Spectral Element Method (SEM) (Patera, 1984), implemented in SPECFEM3D (Komatitsch & Tromp, 2002a, 2002b), to model the low-frequency wavefield from the Gorkha earthquake using a kinematic source (Figure S1 in Supporting Information S1) in an unstructured hexahedral

mesh with 500 m resolution topography (Figure S2 in Supporting Information S1) to better understand the relationships between landslide distribution and ground shaking.

We are limited to rather coarse topography and low frequency (<0.5 Hz) waveforms due to the large size and extent of our modeled region as well as the low frequency content of the modeled seismic source. While higher seismic frequencies are relevant for understanding landslide initiation, particularly for smaller landslides, this low-frequency waveform modeling captures first-order patterns and regional scale topographic amplifications. However, additional higher frequencies would likely modify local amplifications and ground motions for a number of individual landslides, potentially diverging from some of the statistical results. This calls for future, smaller scale, higher frequency studies to increase the understanding of landslide initiation at the local hillslope scale.

2. Data and Methods

2.1. Full Waveform Modeling

To calculate the seismic wavefield from the Gorkha earthquake, we use the software package SPECFEM3D (Komatitsch & Tromp, 2002a, 2002b), which implements the SEM) (Patera, 1984). The SEM uses high-order polynomials to solve the weak form of the wave equation, allowing for the natural incorporation of surface topography and making this an ideal method for investigating the interaction between ground shaking, topography, and landsliding. We represent the rupture as a kinematic source from Wei et al. (2018) that is resolved to 0.5 Hz (Figure S1 in Supporting Information S1). Using this source, we calculate PGV and velocity through time at the free surface in two numerically stable meshes with a 1D velocity model (Table S1 in Supporting Information S1). One mesh has higher resolution (500 m) topography and one has topography that has been smoothed using a moving average with a radius of 20 km (Figure S2 in Supporting Information S1). Both meshes can resolve the seismic wavefield at frequencies up to 1.25 Hz. A comparison between simulations using these two meshes allows us to isolate the effects of topography as a factor of topographic amplification, which is simply the percent difference between the "topography" and "smoothed" peak ground shaking values. See in Supporting Information S1 for further modeling details, including specifics of the mesh and kinematic source (Text S1, Figures S1 and S2 in Supporting Information S1), and validation using high-rate GPS data recorded near the rupture plane during the Gorkha earthquake (Text S2 and Figure S3 in Supporting Information S1). Synthetic waveforms fit the first-order features of the observed data well, although they underestimate peak amplitudes, particularly at high frequencies, indicating our low-frequency modeling is likely underestimating the absolute ground shaking from the earthquake. Several ground motion metrics have been proposed for making comparisons with landslide initiation, including PGA (peak ground acceleration), PGV, duration, and cumulative variables such as Arias Intensity (Jibson et al., 2000; Jibson & Tanyaş, 2020; Nowicki Jessee et al., 2018). For this study, we focus on Horizontal PGV (Figures 1a and S4 in Supporting Information S1), as well as the time evolution of velocity at the free surface (Figure S5 in Supporting Information S1 and Movie S1), because of the low frequencies (<0.5 Hz) that are resolved by our seismic source, the low frequency content of our simulations (<1.25 Hz), and our ability to validate velocity waveforms. We include a metric of cumulative velocity in the supplement (Text S1 and Figure

Figure 1. Tectonic setting of 2015 Gorkha earthquake and coseismic landslides (a) Regional tectonic setting showing the epicenters of the Gorkha mainshock and largest aftershock, red and blue stars, respectively, with red and blue dashed lines showing 2 m slip contours of each rupture (Wei et al., 2018). Red moment tensor shows the GCMT solution for the mainshock. Circles are landslide source areas from Roback et al. (2018), colored by horizontal peak ground velocity (PGV) calculated in this study and scaled by size, defined in legend. Horizontal PGV shakemap from this study in background with same color scale as landslides, black box defines mesh boundaries. Geologic map from DeCelles et al. (2020) overlays the topography, units labeled in the legend. Tethyan Himalayan Sequence (THS), Greater Himalayan Sequence (GHS), Lesser Himalayan Sequence (LHS), and Lesser Himalayan Gondwana Sequence labeled on map. Langtang Valley is highlighted in the black box. White line denotes the transition from gentle topography to the south and steep topography to the north. (b) Shows location of mainshock (red star) and aftershock (blue star) in the context of Nepal. Red regions are major paleo-ruptures - 1505 ~M_w 8.2–8.9,1934 ~M_w 8.4, 1833 ~M_w 7.8 with an indistinguishable rupture area from the 2015 earthquake (Bilham, 2019). Possible seismic gap is denoted in the black dashed polygon. (c) Averages of horizontal PGV, landslide area density, and landslide frequency in 4 km bins across the densest region of landsliding (between the epicenters of the mainshock and aftershock) with respect to lateral distance from the epicenter. Peaks 1, 2, and 3 refer to peaks in landslide area density/frequency and average horizontal PGV colored by most prominent rock unit (GHS - Light Gray, LHS - Light Green). (d) Schematic cross section showing the Main Himalaya Thrust (MHT) and the 2015 epicenter at depth (red star) modified from Bilham (2019). Location of cross section on map denoted with A and A'. Red dashed line approximates the location of the rupture along the MHT. Hatched and thin dashed lines represent the updip seismic gap and region of stable sliding along the detachment at depth, respectively. MHT – Main Himalaya Thrust, MCT – Main Central Thrust, MBT – Main Boundary Thrust, MFT – Main Frontal Thrust, RT – Ramgarh Thrust.

S6 in Supporting Information S1) that accounts for both absolute amplitude and duration. The resulting pattern is very similar to PGV and therefore we do not include the result in the main text.

2.2. Landslide Catalog Processing

Using the Roback et al., 2018 landslide catalog, we determine ground motion, topographic, land use, lithologic, and hillslope position parameters at the locations of the landslide sources, denoted separately from the full landslide area in this catalog. For an expanded discussion of the landslide catalog and explanations for processing choices, see Text S3 in Supporting Information S1. The maximum value of ground shaking parameters (PGV and topographic amplification) from the wavefield simulations and topographic parameters (slope and elevation) from a 30 m SRTM DEM (Farr et al., 2007) within each landslide source area are used for this analysis. In addition, using the 10 m 2020 Esri Global Landcover Database (Karra et al., 2021), we denote if a landslide source is predominantly within a region defined as bare ground or snow and ice to determine if the source area was potentially affected by initiation in glacial terrain, a parameter that has been seen to cause increased amplification of seismic waves (McColl et al., 2012). Lithology plays an important role in landslide initiation; therefore, we also determine if the landslide source is located within either of the two dominant lithologies in this region, the GHS, a set of strong lithologies dominated by high-grade metamorphic gneisses, or the LHS, a weaker lithology dominated primarily by fine-grained sedimentary and low-grade metasedimentary rocks, using the geologic map from DeCelles et al. (2020).

To understand the distribution of landslides along the hillslope, we calculate the normalized distance to rivers ($|d_{st}|$) using equation:

$$|d_{st}| = \frac{d_{st}}{d_{st} + d_{tp}} \tag{1}$$

Here d_{st} is the minimum distance to the river and d_{tp} is the minimum distance to the ridge (i.e., the distance from bottom or top most location on the landslide source polygon, respectively). This relationship yields values between 0 and 1, where 0 is at the river and 1 is at a ridge (Meunier et al., 2008; Rault et al., 2019). Full methodology for how rivers and ridges are defined and location validation, based on the methods of Rault et al., 2019, can be found in Text S4 in Supporting Information S1.

We quantify the relationships between ground motion, topographic parameters, and landslide characteristics by calculating frequency-area distributions (FAD) and slope distributions for subsets of the landslide database. FADs have a distinct power-law behavior, so we can calculate a power-law exponent, α, using the methodology outlined in Clauset et al. (2009) to determine the size-frequency distributions for each subset of the landslide database (Text S5 in Supporting Information S1 for further details) (Figures 2a–2d). Smaller values of α (less negative) and larger values of α (more negative) describe distributions with higher or lower frequency of large landslides, respectively. To demonstrate the distribution of slopes for different subsets of topography and landslides, we calculate the probability distribution function (PDF) of slopes of the topography (P_T) and landslides (P_L) within each dominant geologic unit and within positively and negatively amplified regions (Figure 2e). The slope for each landslide is defined by the maximum slope within each landslide source area from 30 m DEM. By taking the probability ratio of slope distributions of landslides and topography (P_L/P_T) we can quantify how landslides are sampling the slopes with respect to the topographic distribution (Figure 2f). We plot this ratio with respect to the slope minus the topography mode ($S–S_M$) to compare different topographic distributions. This probability ratio shows us whether the distribution within each bin contains slopes for landslides that are more ($P_L/P_T > 1$, oversampling) or less frequent ($P_L/P_T < 1$, undersampling) than the slopes of the topography as a whole. The details of this method and statistical analysis of distributions are outlined in Text S6 in Supporting Information S1 and Marc et al. (2018).

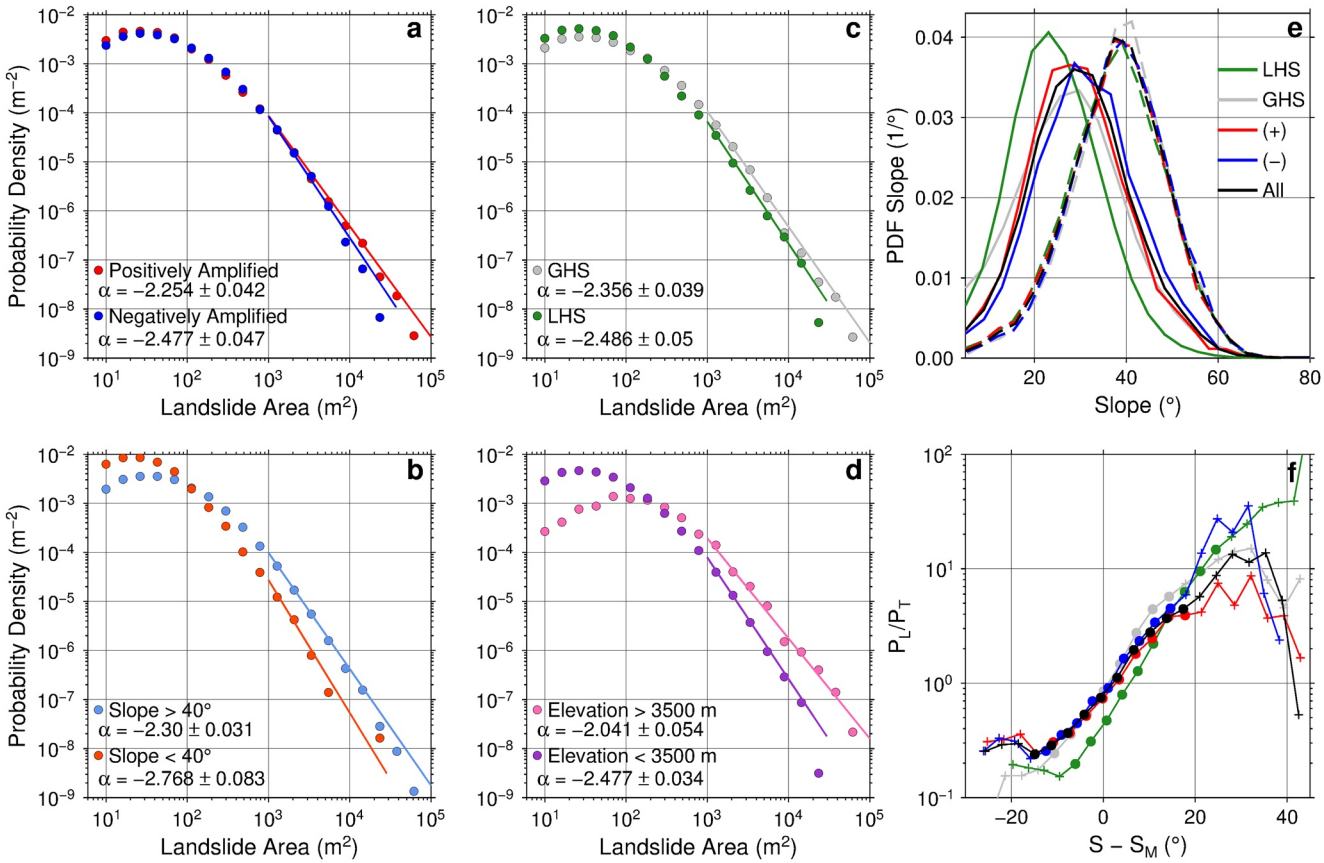

Figure 2. Landslide frequency-area distributions (FAD) and slope distribution. (a–d) FAD for subsets of the landslide source areas in the Roback et al., 2018 database, *N* is the number of landslides used in the calculation of each subset: (a) Positively amplified ($N = 9{,}215$) versus negatively amplified landslides ($N = 10{,}258$) (b) Steep (>40°, $N = 11{,}795$) versus gentle (<40°, $N = 11{,}538$) slopes (c) Greater Himalaya Sequence (GHS) ($N = 9{,}785$) versus Lesser Himalaya Sequence (LHS) ($N = 13{,}058$) (d) high (>3,500 m, $N = 1208$) versus low (<3,500 m, $N = 22{,}125$) elevation. See text for definition of α. (e) Probability density function (PDF) of slopes for topography (P_T, solid line) and landslide sources (P_L, dashed line) for subsets of the landslides including positively and negatively amplified landslides and landslides in GHS and LHS rock units. (f) Probability ratio (P_T/P_L) for each landslide subset. Circles show values that are within 95% confidence interval and crosses indicate bins that do not have sufficient samples to evaluate (Text S6 in Supporting Information S1 for criteria).

3. Results and Discussion

3.1. Controls on Landslide Distribution

The source locations of landslides that followed the 2015 Gorkha earthquake are generally north of the regions with the highest PGV (Figure 1a). This is likely because the highest PGVs from this earthquake were located in the northern part of the Lesser Himalayan physiographic region, where there is comparatively gentle topography that is only capable of producing relatively few and generally smaller landslides (Figure 1a, south of white line) (Frattini & Crosta, 2013; Gallen et al., 2015). North of this transition, topographic relief, slopes, and hillslope lengths increase, due to a ramp on the underlying MHT (Figure 1d), therefore, the terrain becomes more susceptible to landslides, allowing for the triggering of these events even in the presence of relatively smaller ground motions compared to ground shaking south of the white line (Figures 1a and 1c). This shows that within the region affected by strong ground motions, topography has a first-order control on where landslides are triggered.

In addition to this first-order control of topography, slight differences in ground shaking combined with changes in lithology along the length of the rupture likely cause significant variations in landslide triggering. Peaks in landslide frequency and area density are accompanied by a dominant lithologic unit, either LHS or GHS (Figure 1c). The western and eastern peaks (Figure 1c, peaks 1 and 3) in the landslide distribution mostly occur within rocks of the LHS, whereas the central peak (Figure 1c, peak 2) occurs mostly within rocks of the GHS.

Given that ground shaking parameters have the largest values within the longitude range of the GHS (Figure 1c), it may be expected that the frequency of triggered landslides would be highest in this region. The fact that this is not observed may be related to the higher rock strengths and decreased erodibility of the high-grade metamorphic gneisses of the GHS compared to the fine-grained sedimentary and low-grade metasedimentary rocks of the LHS (Cannon et al., 2018). The LHS is dominated by thick phyllite and carbonate units (Kuncha and Galyang Formations and the Lakarpata Group), whereas the GHS is composed of granitic orthogneiss, paragneiss, migmatite, calc-schist and leucogranite, which contribute to the generally greater mechanical strength of the GHS (Cannon et al., 2018).

Topographic amplification at each landslide location provides additional insight into the characteristics of the landslides that were triggered by this event. Horizontal PGV amplification does not appear to have a control on the overall frequency of landsliding at the modeled frequencies, with both a similar slope distribution and number of landslides in both amplified and de-amplified areas. By calculating the relative distance of the landslides along the hillslope, we can better understand the mechanisms of failure and their relationships to topographic amplification. Landslides that are negatively amplified are on average located at the base of hillslopes near rivers. These comparatively weak PGVs can trigger landslides because of high landslide susceptibility within river valleys due to river incision, steep slopes, the effects of groundwater on rock strength, and the common occurences of unconsolidated sediments (Rault et al., 2019; Tseng et al., 2018), (Figure 3b, inset). Of the landslides that are positively amplified, a uniform distribution is observed along the hillslope, primarily on the ridge side facing away from the epicenter of the earthquake, rather than at ridge tops as we might expect from a vertically incident wavefield (Figure 3a, inset). This indicates that a large fraction of these landslides were likely related to the directivity of the rupture, which caused amplification of hillslopes facing away from the incident wavefield. This is a common phenomenon when the wavefield is propagating obliquely to the hillslope, rather than vertically upward beneath the ridge (Maufroy et al., 2015; McColl et al., 2012; Meunier et al., 2008) (Figure S4 in Supporting Information S1). Positively and negatively amplified landslides have very similar slope distributions, showing that neither is preferentially occurring on steeper slopes (Figure 2e).

3.2. Controls on Landslide Size

Rock strength plays an important role in landslide size, with generally larger landslides initiating in stronger rock and smaller landslides only initiating in stronger rock when slopes are steep (Frattini & Crosta, 2013). The GHS, as described above, has a stronger lithology, allowing hillslopes in the GHS to support steeper slopes before failure occurs. This general idea is supported by slope distributions (Figure 2e) and probability ratios (Figure 2f), where GHS has a considerably larger slope mode compared to the LHS (Frattini & Crosta, 2013; Valagussa et al., 2019). From FADs, we can conclude that both GHS rocks and steeper slopes have increased the frequency of larger landslides (Figures 2b and 2c), resulting in the majority of larger, deeper-seated landslides from the Gorkha earthquake. This is also seen as an increase of the landslide area density curve in the GHS compared to landslide frequency, meaning there are larger landslides to accommodate for the decreased landslide frequency in peak 2 of Figure 1c. The occurrence of these larger landslides within the stronger GHS is likely a direct result of the stronger ground shaking in this region associated with the source slip distribution (Figure 1c). This higher amplitude shaking that is low frequency/long wavelength in character can be expected to generate ground motions to deeper depths, corresponding to the failure of deep, large landslides (Bourdeau et al., 2004). Further, calculated probability ratios (P_L/P_T) for LHS and GHS show that landslides in the GHS oversample the slopes of the topography at higher magnitudes than landslides in the LHS (Figure 2f). This continues to support our claim that the topography and landslides in the stronger rocks and steeper slopes of the GHS, along with high PGV values, contribute to the overall distribution of landslide sizes, which has also been shown for other earthquakes (Valagussa et al., 2019). Therefore, ground shaking, in combination with slope and lithology, has a large-scale control on landslide size, with the larger ground shaking values in regions of stronger rock and steeper slopes increasing the frequency of large landslides.

Although topographic amplification does not show a strong control on overall landslide frequency, by comparing positively and negatively amplified landslide FADs (Figure 2a), we show that the distribution of positively amplified landslides has a higher frequency of large landslides. The mechanism for this relationship between increased landslide size and amplification is likely modulated by the topography that is being amplified. The largest landslides occur preferentially in positively amplified areas but also the steepest and highest hillslopes

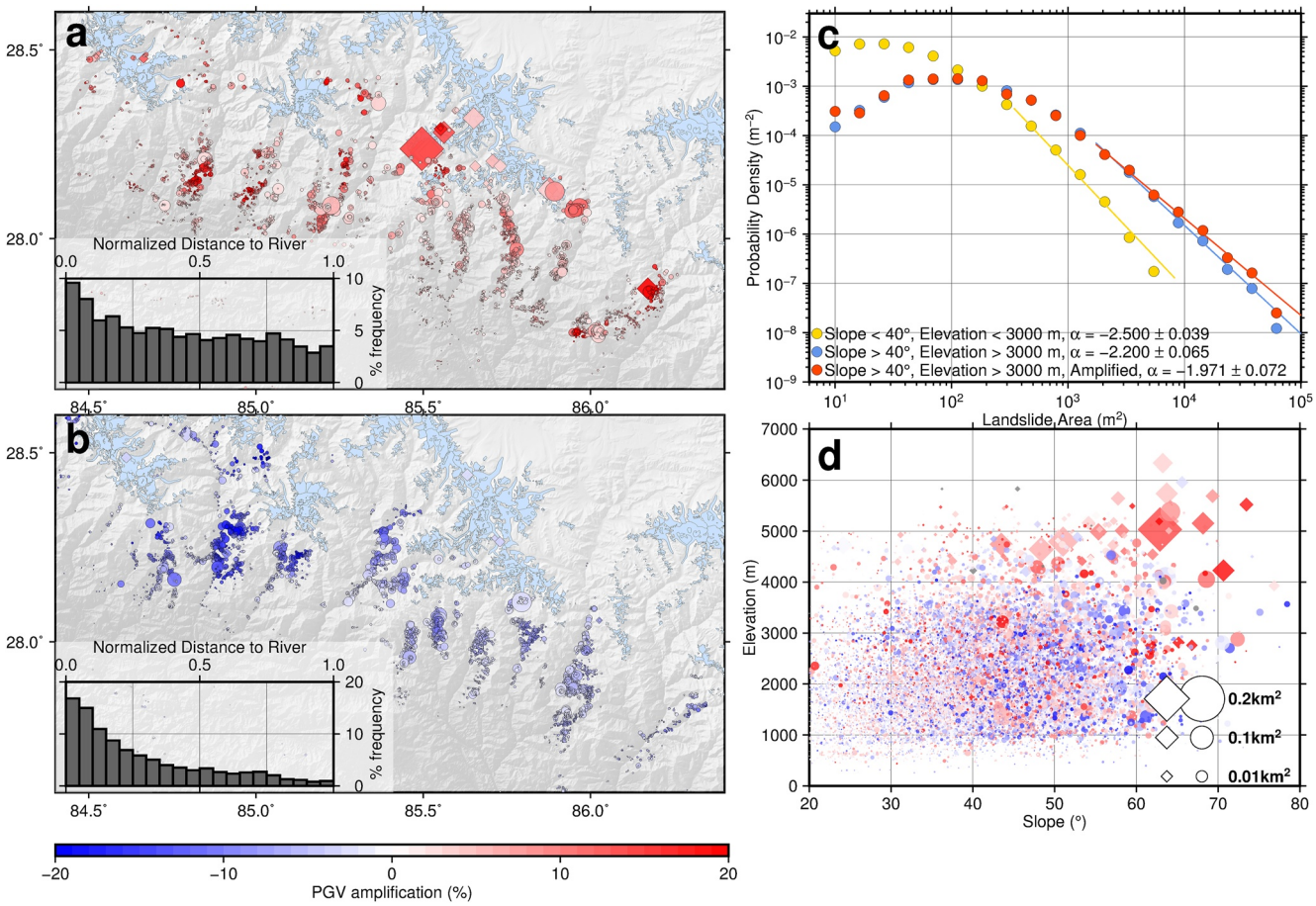

Figure 3. Topographic amplification compared to landslide source size, elevation, and slope (a) Positively amplified landslides (b) negatively amplified landslides. Insets shows histogram of the distribution of positively/negatively amplified landslides with respect to the normalized distance to the closest river (0 is at a river and 1 is at a ridge). Light blue polygons are mapped glaciers since 2008 from the GLIMS database (Raup et al., 2007). Diamonds denote landslides in either a region dominated by bare ground or snow and ice. (c) Frequency-area distributions of landslide source areas with gentle slopes and low elevations (yellow, $N = 10{,}253$), high slopes and high elevations (blue, $N = 2148$), and high slopes, high elevations, and positive amplification ($N = 1042$). N is the number of landslides used to calculate each subset. (d) Scatter plot of elevation versus slope of landslide sources colored by amplification and scaled by landslide source surface area. Legend for symbol size of all plots in panel (c).

(Figure 3c). By plotting FADs of low slopes and low elevations compared to higher slopes and higher elevations, we show that higher slopes and higher elevations have a smaller value of α, therefore a higher frequency of larger landslides (Figure 3c). When we add in positive amplification, the value of α decreases again, that is, increased frequency of large landslides, showing that although slopes and elevations are primary controls on landslide size, topographic amplification also appears to be a secondary control (Figure 3c). Many of these landslides are also associated with glacially sculpted terrain (diamonds in Figures 3a and 3b), which is characterized by steeper, longer hillslopes and can produce deeper-seated landslides than more highly vegetated slopes at lower elevations (McColl et al., 2012; Roback et al., 2018). These ridges are long wavelength topographic features that resonate at lower frequencies, amplifying wavefields that interact with rocks deeper in the subsurface. This combination of resonance and deeper disturbances caused by low frequency seismic waves could be one reason why we see these larger landslides at not only high elevations and steep slopes, but also in regions that are topographically amplified (Bourdeau et al., 2004; Kramer, 1996).

Our conclusion that amplification causes larger landslides, particularly at high elevations, should be taken as a hypothesis to be further confirmed rather than a strongly supported result due to both a mapping and a modeling bias. At high elevations, there is a significant mapping bias toward large landslides, with snow and ice making it difficult to discern small landslide features. The low frequency content of our simulations also presents a

bias, with larger wavelength topography likely having a stronger amplification signal due to the lower resonant frequencies of these features. These larger ridges also have the potential to host larger landslides. Although these results include biases, we provide a hypothesis and motivation to conduct future targeted coseismic landslide mapping efforts and higher frequency modeling studies.

3.3. Langtang Valley Landslide

The largest and most devastating landslide from the 2015 Gorkha earthquake occurred in the Langtang Valley shortly after the initial ground shaking (Figure 1a) (Collins & Jibson, 2015; Fujita et al., 2017; Kargel et al., 2016). The large volume of debris ($\sim 6.95 \times 10^6$ m^3; Lacroix, 2016) and an air blast from the landslide destroyed the village in the Langtang Valley below, killing ~350 people (Kargel et al., 2016). Lacroix (2016) suggested that this devastating event was caused by topographic amplification of the seismic wavefield and the simulations from the current study provide insight into this dynamic process. By integrating velocity amplification through time to show cumulative amplification throughout the rupture, we observe that the source ridge of the Langtang Valley is the most dynamically amplified ridge in the region, other than relatively smaller ridges with gentle slopes to the south (Figure 4d). It is apparent from snapshots of the seismic wavefield and topographic amplification (Figure 4, Movie S1 and S2, Figure S5 in Supporting Information S1) that the ridge experienced multiple amplification episodes throughout the rupture due to the orientation and curvature of this ridge relative to the wavefield. Three major amplification episodes of the ridge occur within the span of ~13 s starting as the initial wavefront passes over the ridge (Figure 4a, episode 1). The wavefront is parallel to the minor ridge axis (Figure 4a, solid arrow) and amplifies the ridge at the kink where it transitions from striking NE to E. After 10 s, a NW propagating wavefront from the E/SE propagating rupture aligns with the major ridge axis (Figure 4b, episode 2, dashed arrow), causing a second episode of amplification. Three seconds following this amplification, a second NW propagating diffuse wavefront amplifies the ridge a third time, again in the orientation of the major ridge axis (Figure 4c, episode 3, dashed arrow). No other ridge in the region experienced more amplification throughout the rupture (Figure 4d), likely due to the orientation of the ridge relative to the wavefield. This orientation perpendicular to the rupture direction, with a curve to the NE, made the ridge susceptible to multiple amplification events as the dominant initial wavefront is aligned and amplifies the ridge along the minor axis (episode 1) and as the rupture continues to propagate, diffuse waves traveling in the opposite direction of the rupture amplify the ridge along the major axis (episode 2 and 3). The three major episodes of amplification overlap with the five source locations of the Langtang Valley landslide (Lacroix, 2016), suggesting that these episodes of amplification, along with the cumulative amplification throughout the rupture, likely promoted the failure of this incredibly devastating mass-wasting event.

3.4. Implications for Future Hazard

As discussed previously, the largest landslides from the Gorkha earthquake occurred at the convergence of steep slopes, high elevations, and positive topographic amplification, typically found in glacially sculpted terrain. This finding has implications for hazards in high mountain regions as climate change continues to cause glaciers to decrease in volume (Maurer et al., 2019; Rounce et al., 2020). Deglaciation can remove the buttressing effect of ice and create gravitationally unstable glacial deposits and cliff faces (e.g., McColl et al., 2012; Richardson & Reynolds, 2000). Ice cover can also act as a buffer to seismic energy and thus can decrease the intensity of surface/near-surface ground shaking (McColl et al., 2012), an effect that wanes with continued deglaciation. Deglaciated topography is also particularly steep, leading to a higher probability of topographic amplification during an earthquake (McColl et al., 2012). Combined, these effects suggest that as these glaciers thin and retreat due to climate change, stronger ground shaking of unstable terrain that can produce larger and more devastating coseismic landslides should be expected from future earthquakes.

Similar to the most recent large seismic events in this region, the 1833 Gorkha earthquake did not rupture to the surface, leaving an up-dip seismic gap (unrelieved stress) that is yet to be filled (Bilham, 2019) (Figures 1b and 1c). Another major Himalayan seismic gap exists west of the Gorkha earthquake rupture, denoted the "central seismic gap", where a major earthquake occurred in 1505 (M ~ 8.2–8.9) from Pokhara westward into the Indian state of Uttarakhand (Bilham, 2019) (Figure 1b). These seismic gaps are where future high-magnitude earth-

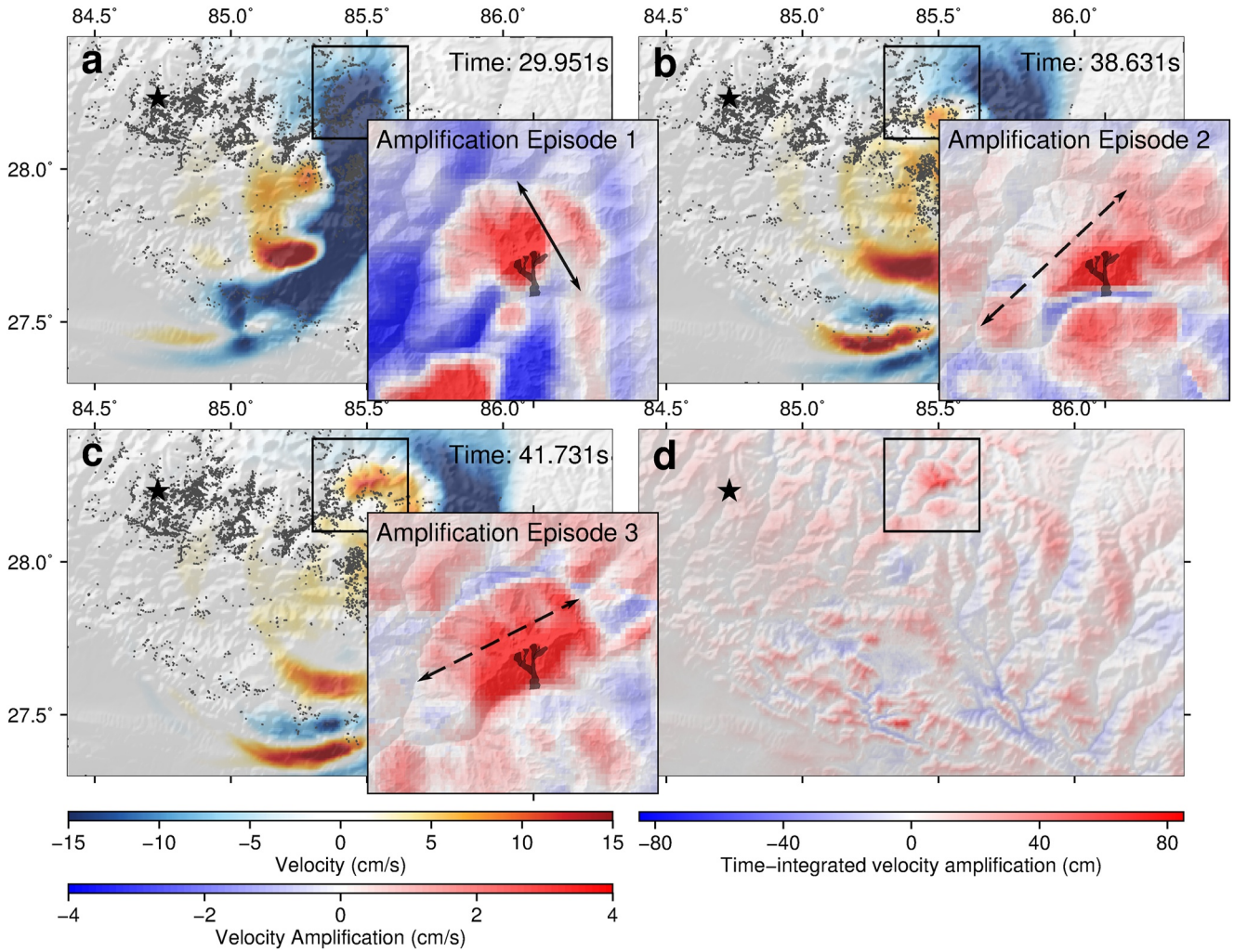

Figure 4. Wavefield and topographic amplification of the source ridge of the Langtang Valley landslide. (a–c) Snapshots of the wavefield at times where the Langtang ridge is amplified due to topography, orange and dark blue are north (+) and south (−) velocity, respectively. Insets show three episodes of amplification at the Langtang ridge colored by velocity amplification, here, the difference between the topography and smoothed simulations. Red and blue are positive and negative amplification, respectively. Landslide outline from Lacroix, 2016 is shown in the inset as black polygons. Arrows designate the direction along the wavefronts that caused ridge amplification and are perpendicular to the wavefront propagation direction. Solid and dashed arrows designate wavefronts parallel to the minor and major ridge axes, respectively. (d) Time integrated velocity amplification. Amplification here is the difference between the velocity of the topography and smoothed simulations. Black star is Gorkha epicenter. Black square highlights the Langtang valley.

quakes in the range of M_w 7.5–8.0 are likely anytime in the remaining 21st or 22nd centuries. Probabilistic modeling of potential ground shaking and topographic amplification from future earthquakes, similar to the approach taken in this study, may provide important insights into future coseismic landslide hazards in these regions of high seismic potential, particularly in regions experiencing deglaciation.

4. Conclusions

This study has investigated the relationship between the characteristics of coseismic landslides and ground shaking from the 2015 Gorkha earthquake. Low-frequency seismic wavefield simulations reveal that PGV, rock strength, and slope are important for the large-scale distribution of landslides. These factors, along with topographic amplification and high elevations, contribute to higher frequencies of large landslides. In particular, we find that the largest landslides occur where there is high topographic amplification, steep slopes, and high elevations, typified by glacially sculpted terrain. We also observe that dynamic amplification of the Langtang Valley

source ridge due to the orientations of successive wavefronts from different portions of the Gorkha rupture likely contributed to the triggering of this large and devastating landslide. This work has important implications for future hazards in seismically active high mountain terrain. As glaciers continue to thin and retreat due to climate change, we may expect both decreased stability of deglaciated or partially deglaciated terrain and increased ground shaking from site amplification from future earthquakes, leading to a potential increase in the frequency of large coseismic landslides. Quantifying ground shaking and topographic amplification in the context of evolving landscape properties can provide an important tool for assessing coseismic landslide potential in the Himalaya and other active mountain regions.

Data Availability Statement

The data and software used in the simulations included (a) a finite fault model from Wei et al., 2018, found in the supplementary material of that paper, (b) 30m topographic data that was provided by SRTM3 (https://doi.org/10.1029/2005RG000183) and distributed by GMTSAR (https://topex.ucsd.edu/gmtsar/demgen/), this topography was also used in the analysis, and (c) open source software SPECFEM3D cartesian (Komatitsch & Tromp, 2002a, 2002b) distributed by Computational Infrastructure for Geophysics (https://geodynamics.org/resources/notebooks). The landslide database is from Roback et al., 2018 (https://doi.org/10.1016/j.geomorph.2017.01.030) and is available from https://doi.org/10.5066/F7DZ06F9. Landcover data used in the present study is distributed by ESRI and is based on the data set produced for the Dynamic World Project by National Geographic Society in partnership with Google and the World Resources Institute (https://tiledimageservices.arcgis.com/P3ePLMYs2RVChkJx/arcgis/rest/services/Esri_2020_Land_Cover_V2/ImageServer). Glaciers outlines were taken from the GLIMS database (https://www.glims.org/).

Acknowledgments
This study was supported by the NASA Interdisciplinary Science program, Grant 80NSSC18K0432. We would also like to thank Odin Marc and an anonymous reviewer for their helpful comments and revisions. C. S. Watson was supported by the UKRI GCRF Urban Disaster Risk Hub (NE/S009000/1) (Tomorrow's Cities), and the Centre for the Observation and Modelling of Earthquakes, Volcanoes and Tectonics. P. G. DeCelles acknowledges NSF-Tectonics grant EAR1763432.

References

Asimaki, D., & Mohammadi, K. (2018). On the complexity of seismic waves trapped in irregular topographies. *Soil Dynamics and Earthquake Engineering*, *114*, 424–437. https://doi.org/10.1016/j.soildyn.2018.07.020

Avouac, J.-P., Meng, L., Wei, S., Wang, T., & Ampuero, J. P. (2015). Lower edge of locked Main Himalayan Thrust unzipped by the 2015 Gorkha earthquake. *Nature Geoscience*, *8*(9), 708–711. https://doi.org/10.1038/ngeo2518

Bilham, R. (2019). *Himalayan earthquakes: A review of historical seismicity and early 21st century slip potential* (p. 483). Geological Society,Special Publications. https://doi.org/10.1144/sp483.16

Bourdeau, C., Havenith, H.-B., Fleurisson, J.-A., & Grandjean, G. (2004). *Numerical modelling of seismic slope stability*. Springer. https://doi.org/10.1007/978-3-540-39918-6_74

Cannon, J. M., Murphy, M. A., & Taylor, M. (2018). Segmented strain accumulation in the High Himalaya expressed in river channel steepness. *Geosphere*, *14*(3), 1131–1149. https://doi.org/10.1130/GES01508.1

Clauset, A., Shalizi, C. R., & Newman, M. E. J. (2009). Power-law distributions in empirical data. *Society for Industrial and Applied Mathematics*, *51*(4), 661–703. https://doi.org/10.1137/070710111

Collins, B. D., & Jibson, R. W. (2015). *Assessment of existing and potential landslide hazards resulting from the April 25, 2015 Gorkha, Nepal earthquake sequence*. Open-File Report. https://doi.org/10.3133/ofr20151142

DeCelles, P. G., Carrapa, B., Ojha, T. P., Gehrels, G. E., & Collins, D. (2020). *Structural and Thermal Evolution of the Himalayan Thrust Belt in Midwestern Nepal*. Geological Society of America Special Paper, (Vol. 547, pp. 1–78). https://doi.org/10.1130/2020.2547

Fan, W., & Shearer, P. M. (2015). Detailed rupture imaging of the 25 April 2015 Nepal earthquake using teleseismic P waves. *Geophysical Research Letters*, *42*(14), 5744–5752. https://doi.org/10.1002/2015GL064587

Farr, T. G., Rosen, P. A., Caro, E., Crippen, R., Duren, R., Hensley, S., et al. (2007). The shuttle radar topography mission. *Reviews of Geophysics*, *45*(2), 1–33. https://doi.org/10.1029/2005RG000183

Frattini, P., & Crosta, G. B. (2013). The role of material properties and landscape morphology on landslide size distributions. *Earth and Planetary Science Letters*, *361*, 310–319. https://doi.org/10.1016/J.EPSL.2012.10.029

Fujita, K., Inoue, H., Izumi, T., Yamaguchi, S., Sadakane, A., Sunako, S., et al. (2017). Anomalous winter-snow-amplified earthquake-induced disaster of the 2015 Langtang avalanche in Nepal. *Natural Hazards and Earth System Sciences*, *17*(5), 749–764. https://doi.org/10.5194/NHESS-17-749-2017

Gallen, S. F., Clark, M. K., & Godt, J. W. (2015). Coseismic landslides reveal near-surface rock strength in a high-relief, tectonically active setting. *Geology*, *43*(1), 11–14. https://doi.org/10.1130/G36080.1

Hartzell, S. H., Ramírez-Guzmán, L., Meremonte, M., & Leeds, A. (2017). Ground motion in the presence of complex topography II: Earthquake sources and 3D simulations. *Bulletin of the Seismological Society of America*, *107*(1), 344–358. https://doi.org/10.1785/0120160159

Hubbard, J., Almeida, R., Foster, A., Sapkota, S. N., Burgi, P., & Tapponnier, P. (2016). Structural segmentation controlled the 2015 Mw 7.8 Gorkha earthquake rupture in Nepal. *Geology*, *44*(8), 639–642. https://doi.org/10.1130/G38077.1

Jibson, R. W., Harp, E. L., & Michael, J. A. (2000). A method for producing digital probabilistic seismic landslide hazard maps. *Engineering Geology*, *58*(3–4), 271–289. https://doi.org/10.1016/S0013-7952(00)00039-9

Jibson, R. W., & Tanyaş, H. (2020). The influence of frequency and duration of seismic ground motion on the size of triggered landslides—a regional view. *Engineering Geology*, *273*, 105671. https://doi.org/10.1016/J.ENGGEO.2020.105671

Kargel, J. S., Leonard, G. J., Shugar, D. H., Haritashya, U. K., Bevington, A., Fielding, E. J., et al. (2016). Geomorphic and geologic controls of geohazards induced by Nepal's 2015 Gorkha earthquake. *Science (New York, N.Y.)*, *351*(6269), 1–18. https://doi.org/10.1126/science.aac8353

Karra, K., Kontgis, C., Statman-Weil, Z., Mazzariello, J. C., Mathis, M., & Brumby, S. P. (2021). *Global land use/ land cover with Sentinel 2 and deep learning* (pp. 4704–4707). https://doi.org/10.1109/IGARSS47720.2021.9553499

Keefer, D. K. (2002). Investigating landslides caused by earthquakes - a historical review. *Surveys in Geophysics*, *23*(6), 473–510. https://doi.org/10.1023/A:1021274710840

Komatitsch, D., & Tromp, J. (2002a). Spectral-element simulations of global seismic wave propagation - I. Validation. *Geophysical Journal International*, *149*(2), 390–412. https://doi.org/10.1046/j.1365-246X.2002.01653.x

Komatitsch, D., & Tromp, J. (2002b). Spectral-element simulations of global seismic wave propagation - II. Three-dimensional models, oceans, rotation and self-gravitation. *Geophysical Journal International*, *150*(1), 303–318. https://doi.org/10.1046/j.1365-246X.2002.01716.x

Kramer, S. L. (1996). *Geotechnical earthquake engineering*. Prentice-Hall.

Lacroix, P. (2016). Landslides triggered by the Gorkha earthquake in the Langtang valley, volumes and initiation processes. *Earth Planets and Space*, *68*(1), 1–10. https://doi.org/10.1186/s40623-016-0423-3

Lee, S.-J., Chan, Y. C., Komatitsch, D., Huang, B. S., & Tromp, J. (2009). Effects of realistic surface topography on seismic ground motion in the Yangminshan region of Taiwan based upon the spectral-element method and LiDAR DTM. *Bulletin of the Seismological Society of America*, *99*(2A), 681–693. https://doi.org/10.1785/0120080264

Marc, O., Stumpf, A., Malet, J. P., Gosset, M., Uchida, T., & Chiang, S. H. (2018). Initial insights from a global database of rainfall-induced landslide inventories: The weak influence of slope and strong influence of total storm rainfall. *Earth Surface Dynamics*, *6*(4), 903–922. https://doi.org/10.5194/ESURF-6-903-2018

Maufroy, E., Cruz-Atienza, V. M., Cotton, F., & Gaffet, S. (2015). Frequency-scaled curvature as a proxy for topographic site-effect amplification and ground-motion variability. *Bulletin of the Seismological Society of America*, *105*(1), 354–367. https://doi.org/10.1785/0120140089

Maurer, J. M., Schaefer, J. M., Rupper, S., & Corley, A. (2019). Acceleration of ice loss across the Himalayas over the past 40 years. *Science Advances*, *5*(6), 1–12. https://doi.org/10.1126/sciadv.aav7266

McColl, S. T., Davies, T. R. H., & McSaveney, M. J. (2012). The effect of glaciation on the intensity of seismic ground motion. *Earth Surface Processes and Landforms*, *37*(12), 1290–1301. https://doi.org/10.1002/esp.3251

Meunier, P., Hovius, N., & Haines, J. A. (2008). Topographic site effects and the location of earthquake induced landslides. *Earth and Planetary Science Letters*, *275*(3–4), 221–232. https://doi.org/10.1016/j.epsl.2008.07.020

Nowicki Jessee, M. A., Hamburger, M. W., Allstadt, K., Wald, D. J., Robeson, S. M., Tanyaş, H., et al. (2018). A global empirical model for near-real-time assessment of seismically induced landslides. *Journal of Geophysical Research: Earth Surface*, *123*(8), 1835–1859. https://doi.org/10.1029/2017JF004494

Patera, A. T. (1984). A spectral element method for fluid dynamics: Laminar flow in a channel expansion. *Journal of Computational Physics*, *54*(3), 468–488. https://doi.org/10.1016/0021-9991(84)90128-1

Petley, D. N. (2012). Global patterns of loss of life from landslides. *Geology*, *40*(10), 927–930. https://doi.org/10.1130/G33217.1

Rault, C., Chao, W.-A., Gelis, C., Burtin, A., Chang, J.-M., Marc, O., et al. (2020). Seismic response of a mountain ridge prone to landsliding. *Bulletin of the Seismological Society of America*, *110*(6), 3004–3020. https://doi.org/10.1785/0120190127

Rault, C., Robert, A., Marc, O., Hovius, N., & Meunier, P. (2019). Seismic and geologic controls on spatial clustering of landslides in three large earthquakes. *Earth Surface Dynamics*, *7*(3), 829–839. https://doi.org/10.5194/esurf-7-829-2019

Raup, B., Racoviteanu, A., Khalsa, S. J. S., Helm, C., Armstrong, R., & Arnaud, Y. (2007). The GLIMS geospatial glacier database: A new tool for studying glacier change. *Global and Planetary Change*, *56*(1–2), 101–110. https://doi.org/10.1016/J.GLOPLACHA.2006.07.018

Richardson, S. D., & Reynolds, J. M. (2000). An overview of glacial hazards in the Himalayas. *Quaternary International*, *65–66*, 31–47. https://doi.org/10.1016/S1040-6182(99)00035-X

Roback, K., Clark, M. K., West, A. J., Zekkos, D., Li, G., Gallen, S. F., et al. (2018). The size, distribution, and mobility of landslides caused by the 2015 Mw 7.8 Gorkha earthquake, Nepal. *Geomorphology*, *301*, 121–138. https://doi.org/10.1016/J.GEOMORPH.2017.01.030

Rounce, D. R., Hock, R., & Shean, D. E. (2020). Glacier mass change in high mountain Asia through 2100 using the open-source Python glacier evolution model (PyGEM). *Frontiers of Earth Science*, *7*, 331. https://doi.org/10.3389/feart.2019.00331

Tseng, C.-M., Chen, Y.-R., & Wu, S.-M. (2018). Scale and spatial distribution assessment of rainfall-induced landslides in a catchment with mountain roads. *Natural Hazards and Earth System Sciences*, *18*(2), 687–708. https://doi.org/10.5194/nhess-18-687-2018

Valagussa, A., Marc, O., Frattini, P., & Crosta, G. B. (2019). Seismic and geological controls on earthquake-induced landslide size. *Earth and Planetary Science Letters*, *506*, 268–281. https://doi.org/10.1016/J.EPSL.2018.11.005

Wei, S., Chen, M., Wang, X., Graves, R., Lindsey, E., Wang, T., et al. (2018). The 2015 Gorkha (Nepal) earthquake sequence: I. Source modeling and deterministic 3D ground shaking. *Tectonophysics*, *722*, 447–461. https://doi.org/10.1016/J.TECTO.2017.11.024

References From the Supporting Information

Aki, K., & Richards, P. G. (2002). *Quantitative seismology* (2nd edn.). University Science Books.

Ashford, S. A., Sitar, N., Lysmer, J., & Deng, N. (1997). Topographic effects on the seismic response of steep slopes. *Bulletin of the Seismological Society of America*, *87*, 692–700. https://doi.org/10.1785/bssa0870030692

Bouchon, M. (1985). A simple, complete numerical solution to the problem of diffraction of SH waves by an irregular surface. *Journal of the Acoustical Society of America*, *77*(1), 1–5. https://doi.org/10.1121/1.392258

Bouchon, M., Schultz, C. A., & Toksöz, M. N. (1996). Effect of three-dimensional topography on seismic motion. *Journal of Geophysical Research*, *101*(B3), 5835–5846. https://doi.org/10.1029/95jb02629

Galetzka, J., Melgar, D., Genrich, J. F., Geng, J., Owen, S., Lindsey, E. O., et al. (2015). Maharjan, NSlip pulse and resonance of the Kathmandu basin during the 2015 Gorkha earthquake, Nepal. *Science*, *349*(6252), 1091–1095. https://doi.org/10.1126/science.aac6383

Komatitsch, D., & Tromp, J. (1999). Introduction to the spectral element method for three-dimensional seismic wave propagation. *Geophysical Journal International*, *139*(3), 806–822. https://doi.org/10.1046/j.1365-246X.1999.00967.x

Komatitsch, D., & Vilotte, J.-P. (1998). The spectral element method: An efficient tool to simulate the seismic response of 2D and 3D geological structures. *Bulletin of the Seismological Society of America*, *88*(2), 368–392. Retrieved from https://pubs.geoscienceworld.org/ssa/bssa/article-pdf/88/2/368/2709303/BSSA0880020368.pdf

Lee, S.-J., Komatitsch, D., Huang, B. S., & Tromp, J. (2009). Effects of topography on seismic-wave propagation: An example from Northern Taiwan. *Bulletin of the Seismological Society of America*, *99*(1), 314–325. https://doi.org/10.1785/0120080020

Mahesh, P., Rai, S. S., Sivaram, K., Paul, A., Gupta, S., Sarma, R., & Gaur, V. K. (2013). One-dimensional reference velocity model and precise locations of earthquake hypocenters in the Kumaon-Garhwal Himalaya. *Bulletin of the Seismological Society of America*, *103*(1), 328–339. https://doi.org/10.1785/0120110328

Marc, O., Behling, R., Andermann, C., Turowski, J. M., Roessner, S., & Hovius, N. (2019). Long-term erosion of the Nepal Himalayas by bedrock landsliding: The role of monsoons, earthquakes and giant landslides. *Earth Surface Dynamics*, *7*(1), 107–128. https://doi.org/10.5194/esurf-7-107-2019

Martha, T. R., Roy, P., Mazumdar, R., Govindharaj, K. B., & Kumar, K. V. (2017). Spatial characteristics of landslides triggered by the 2015 Mw 7.8 (Gorkha) and Mw 7.3 (Dolakha) earthquakes in Nepal. *Landslides*, *14*(2), 697–704. https://doi.org/10.1007/s10346-016-0763-x

Stark, C. P., & Guzzetti, F. (2009). Landslide rupture and the probability distribution of mobilized debris volumes. *Journal of Geophysical Research*, *114*(F2), F00A02. https://doi.org/10.1029/2008JF001008

Tanyaş, H., Van Westen, C. J., Allstadt, K. E., & Jibson, R. W. (2018). Factors controlling landslide frequency-area distributions. *Earth Surface Processes and Landforms*, *44*(4), 900–917. https://doi.org/10.1002/esp.4543

Tsou, C.-Y., Chigira, M., Higaki, D., Sato, G., Yagi, H., Sato, H. P., et al. (2018). Topographic and geologic controls on landslides induced by the 2015 Gorkha earthquake and its aftershocks: An example from the Trishuli valley, central Nepal. *Landslides*, *15*(5), 953–965. https://doi.org/10.1007/s10346-017-0913-9

Xu, C. (2018). Landslides triggered by the 2015 Gorkha, Nepal earthquake. *The International Archives of the Photogrammetry, Remote Sensing and Spatial Information Sciences*, *XLII*, 1989–1993. https://doi.org/10.5194/isprs-archives-XLII-3-1989-2018